Average and Small-Signal Model of the Four-Switch Buck-Boost Converter under both Duty-Cycle and Phase-Shift Modulation

Ezio Gallo*, Filip Cvejić†, Giorgio Spiazzi†, Davide Biadene*, and Tommaso Caldognetto*
*Dept. of Management and Engineering (DTG)
University of Padova, Vicenza, Italy
Email: ezio.gallo@phd.unipd.it, davide.biadene@unipd.it, tommaso.caldognetto@unipd.it
†Dept. of Information Engeneering (DEI)
University of Padova, Padova, Italy
Email: filip.cvejic@unipd.it, giorgio.spiazzi@dei.unipd.it

***Abstract*—The four-switch buck-boost (FSBB) topology is often used in combination with other isolated converters to extend the voltage range capability of the overall structure. In such applications, the duty-cycles of the two legs of the FSBB are independently controlled, and a phase-shift is introduced in order to shape the inductor current ripple and thus achieve zero voltage switching. This paper proposes a non-linear average model, and the corresponding linearized small-signal model, for the FSBB operated in the described way. The derived average and small-signal models are shown to be in excellent agreement with simulation and are also validated by measurements on an experimental prototype.**

***Index Terms*—four-switch buck-boost, average model, small-signal model.**

I. Introduction

THE four-switch Buck-Boost (FSBB) topology, shown in Fig. 1, is a well-known non-inverting step-up/down topology, which is used in combination with other isolated converters for higher input/output voltage ranges. Examples of such application are reported in [1]– [4], where one switching leg is shared with a constant frequency half-bridge LLC stage, employed as an isolated DC transformer with a fixed voltage gain. In [4], the FSBB is used with an LLC stage with a diode rectifier, and it allows for an almost constant operating frequency of the LLC stage over a wide output voltage range. In these applications, one of the leg is operated at a fixed duty-cycle of 50%, leaving the duty-cycle of the other leg as the only control variable for voltage gain regulation. However, a second degree of freedom is represented by the phase-shift between the driving signals of the two legs, which can be used to properly shape the inductor current waveform, so as to achieve full Zero-Voltage-Switching (ZVS) operation.

Despite the simple structure of the FSBB, the literature lacks a model that covers the dynamics of the converter during the above described operation. Typical FSBB average models account for Buck or Boost operating modes, where only one of the two legs is modulated to reach the desired output voltage, or operating in buck-boost mode where S_{1t} and S_{3t} are turned on and off simultaneously [5], [6].

In [7] a control strategy that utilizes buck-boost operation for a smooth transition between the buck and boost modes is presented. This strategy is used in [8], where a single small-signal model for the FSBB in all three operation modes is derived. However, the effect of the phase-shift, present in the buck-boost mode, is neglected. Furthermore, no results are provided in the buck-boost mode.

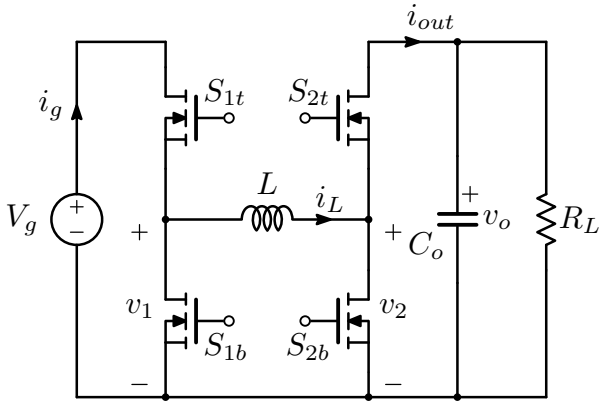

Fig. 1. Four-switch buck-boost converter schematic.

The aim of this paper is to develop a suitable non-linear average model for the converter in Fig. 1 in the most general case, where both input and output legs operate with independent duty-cycles, and the phase-shift between the two legs is used for inductor RMS current minimization and ZVS range maximization. From the non-linear average model, a simple linearization technique is used to derive the desired small-signal linear model, using which, the converter dynamics can be analyzed.

In Section II, the converter modes of operation are reviewed. In Section III both average and small-signal models of the converter are shown, presenting the somewhat unusual approach used for the derivation. Section IV addresses the

verification of the models by simulation of the switching circuit in Matlab/Simulink. Finally, in Section V the output duty-cycle to output voltage transfer function is verified with experimental measurements.

II. Review of the converter's modes of operation

An example of the waveforms of the converter operated as previously explained is displayed in Fig. 2. D_g and D_o are defined as the duty cycles of the top mosfet of the input and output leg respectively (denoted as S_{1t} and S_{2t} of the Fig. 1) . The standard way to define the phase-shift, as the relative time between the center points of two voltage waveforms $v_1(t)$ and $v_2(t)$, is here denoted by β, and is positive when v_2 leads v_1. Note that, in order to simplify the analytical derivations in Section III, the overlap δ_2 between v_1 and v_2 is used as the control variable instead of β.

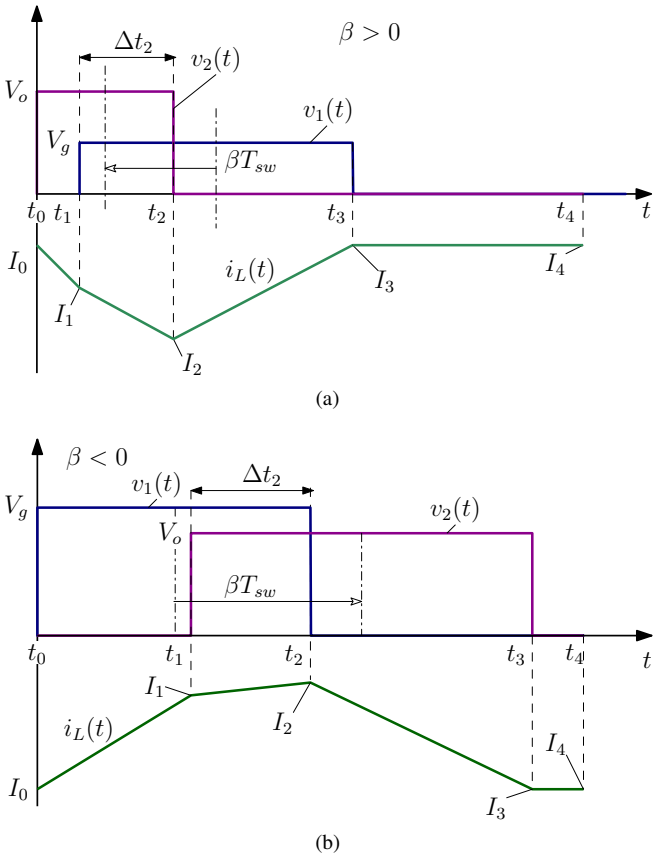

Fig. 2. Example of converter waveforms for different phase-shift values. (a) Region 2 in step-up case ($D_o < 0.5$); (b) Region 8 in step-down case ($D_o > 0.5$).

It can be derived from the volt-second balance of the inductor that the voltage gain is a function only of the two duty-cycles. Thus, the phase-shift can be used to properly shape the piece-wise linear current waveform $i_L(t)$ to achieve ZVS of the four switches, as well as minimization of its RMS value. Depending on the phase-shift β, four different modes are possible for each of the step-up or step-down cases; boundary regions are reported in Fig. 3 for two different values of input duty-cycle D_g. A proper design should avoid operation in regions 1 and 5, because of the lack of a complete ZVS condition. In this paper the analysis is focused on regions 2-6 and 4-8, since these make it possible to achieve ZVS turn-on transition for all four switches by modulating the phase-shift.

In each region of operation, the switching period can be divided into four different sub-periods Δt_k. In (1) the sub-periods and their normalized duration are described as function of the two duty-cycles and the phase-shift β.

$$\Delta t_k = t_k - t_{k-1} \quad \Rightarrow \quad \delta_k = \frac{\Delta t_k}{T_{sw}} = f(d_g, d_o, \beta). \tag{1}$$

The corresponding inductor current piece-wise linear waveform can be described by the following:

$$I_k = I_{k-1} + \frac{\delta_k}{L} V_{Lk} \quad (k = 1, 2, 3, 4), \tag{2}$$

where V_{Lk} is the voltage across the inductor L during the k-th sub-period. Expressions (1) and (2) will be the foundation of the derivation in the following section.

III. Average Non-Linear and Small-Signal Models

In order to understand the dynamic behaviour of the inductor in the FSBB, the waveforms of interest are provided in Fig. 4 for operation in region 4-8. There, it is shown that a variation of the overlap (which is the normalized duration δ_2 defined by (1)), causes a change in the inductor voltage waveform v_L. This results in a finite impulse response of the averaged inductor voltage defined by:

$$\bar{v}_L(\tau) = \frac{1}{T_{sw}} \int_{\tau - \frac{T_{sw}}{2}}^{\tau + \frac{T_{sw}}{2}} v_L(t) dt. \tag{3}$$

In response to the voltage variation the inductor current will change its moving average value according to:

$$L \frac{d}{dt} \bar{i}_L = \bar{v}_L = d_g v_g - d_o v_o + v_{FIR}(t, d_g, d_o, \delta_2^k, \delta_2^{k+1}) \tag{4}$$

where v_{FIR} describes the finite impulse response of the averaged inductor voltage. In order to derive a model that can provide an insight into the behaviour of the FSBB, the dynamics introduced by v_{FIR} are neglected in the following steps, avoiding additional complexity.[1] On the other hand, the effect of v_{FIR} on $\bar{i}_L$ cannot be so easily neglected, since it causes a permanent change. This leads to the necessity for defining a new state variable, $\bar{i}_e$, described by:

$$\bar{v}_L \approx \bar{v}_{Le} = d_g v_g - d_o v_o = L \frac{d}{dt} \bar{i}_e. \tag{5}$$

The key point is that the new state variable, $\bar{i}_e$, takes into account only the average voltage that is not phase-shift (overlap) dependent. Fig. 4, which is given for region 4-8, also highlights the fact that changing only δ_2 results in no change of the bottom envelope of the current. Similarly, the top envelope remains unchanged in the case of region 2-6. This, along with the fact that from (4) it can be shown that:

$$I_4 - I_0 = \frac{d_g v_g - d_o v_o}{f_{sw} L} \tag{6}$$

[1]The derivation of the model without neglecting the effect of v_{FIR} might be addressed in future work.

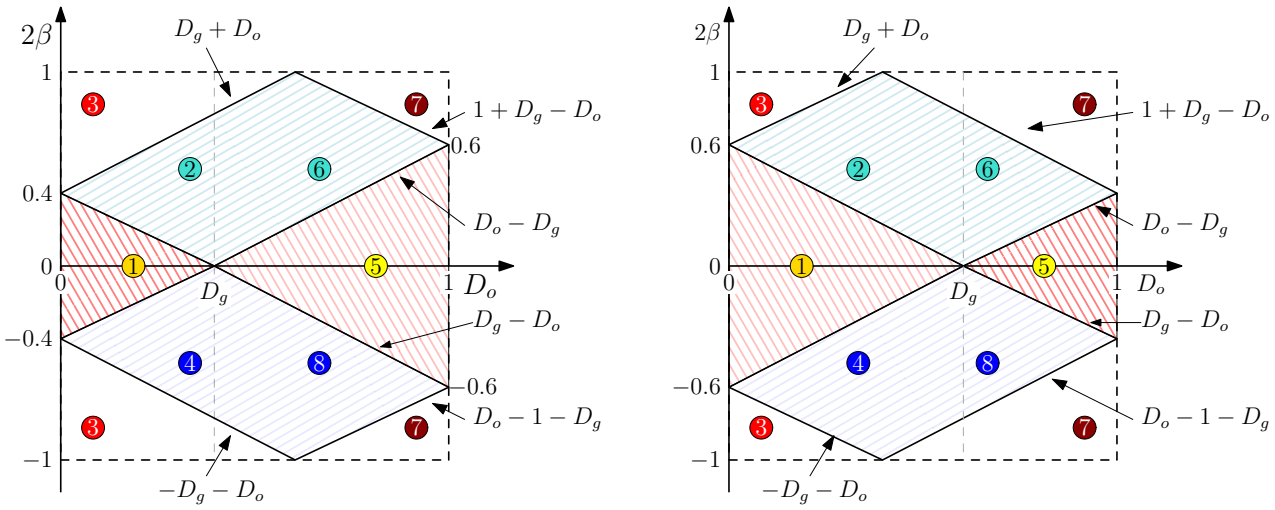

Fig. 3. Mode boundaries for $D_g = 0.4$ and $D_g = 0.6$.

naturally leads to:

$$\bar{i}_e = \frac{I_0 + I_4}{2} \Rightarrow \begin{cases} I_0 & = \bar{i}_e - \dfrac{d_g v_g - d_o v_o}{2 f_{sw} L} \\ I_4 & = \bar{i}_e + \dfrac{d_g v_g - d_o v_o}{2 f_{sw} L} \end{cases} \tag{7}$$

It should be noted that the approximation introduced in (5) is related to the assumption that δ_2 changes during Δt_4, as it does in Fig. 4. A different assumption of the instant when δ_2 changes would result in somewhat different expressions, but the performance of the model should remain the same.

The input and output current can be found by considering the trapezoidal areas of the current waveform in Fig. 2 as follows, for regions 4-8 and 2-6, respectively:

$$R\,4-8: \begin{cases} \bar{i}_g & = \displaystyle\sum_{k=1}^{2} \delta_k \frac{I_{k-1} + I_k}{2} \\ \bar{i}_{out} & = \displaystyle\sum_{k=2}^{3} \delta_k \frac{I_{k-1} + I_k}{2} \end{cases} \tag{8}$$

$$R\,2-6: \begin{cases} \bar{i}_g & = \displaystyle\sum_{k=2}^{3} \delta_k \frac{I_{k-1} + I_k}{2} \\ \bar{i}_{out} & = \displaystyle\sum_{k=1}^{2} \delta_k \frac{I_{k-1} + I_k}{2} \end{cases} \tag{9}$$

Using equation (7), the above equations can be rearranged as in (10) and (11).

$$R\,4-8: \begin{cases} \bar{i}_g & = \bar{i}_e d_g + \dfrac{v_o d_o d_g}{2 f_{sw} L} - \dfrac{v_o \delta_2}{2 f_{sw} L} \\ \bar{i}_{out} & = \bar{i}_e d_o + \dfrac{v_g d_o d_g}{2 f_{sw} L} - \dfrac{v_g \delta_2}{2 f_{sw} L} \end{cases} \tag{10}$$

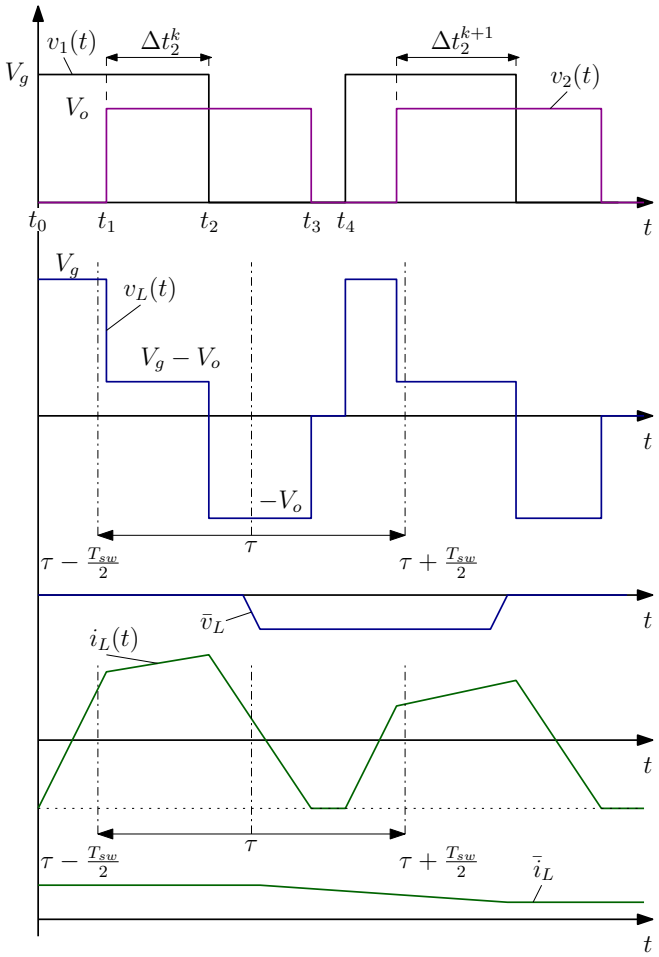

Fig. 4. Instantaneous and moving average waveforms on the inductor L in region 4-8. The changing of the overlap δ_2 generates a step response on the average voltage $\bar{v}_L$ that causes a variation on the inductor current i_L and thus in its average value $\bar{i}_L$.

TABLE I
SMALL SIGNAL PARAMETERS OF THE INPUT AND THE OUTPUT CURRENTS IN THE CONSIDERED REGIONS

Region	a_g	b_g	g_g	e_g	a_o	b_o	g_o	e_o
4-8	$\frac{V_o D_g}{2f_{sw}L}$	$-\frac{V_o \delta_2}{f_{sw}L}$	$-\frac{\delta_2 - D_g D_o}{2f_{sw}L}$	$\bar{i}_e + \frac{V_o D_o}{2f_{sw}L}$	$\bar{i}_e + \frac{V_g D_g}{2f_{sw}L}$	$-\frac{V_g \delta_2}{2f_{sw}L}$	$\frac{\delta_2 - D_g D_o}{2f_{sw}L}$	$\frac{D_o V_g}{2f_{sw}L}$
2-6	$-\frac{V_o D_g}{2f_{sw}L}$	$\frac{V_o \delta_2}{f_{sw}L}$	$\frac{\delta_2 - D_g D_o}{2f_{sw}L}$	$\bar{i}_e - \frac{V_o D_o}{2f_{sw}L}$	$\bar{i}_e - \frac{V_g D_g}{2f_{sw}L}$	$\frac{V_g \delta_2}{2f_{sw}L}$	$-\frac{\delta_2 - D_g D_o}{2f_{sw}L}$	$-\frac{D_o V_g}{2f_{sw}L}$

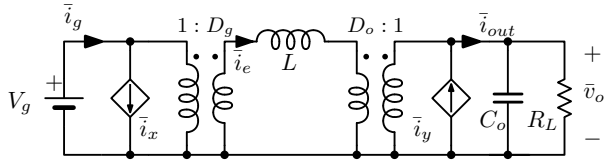

Fig. 5. Non-linear average model of the FSBB in the Regions 2-6 and 4-8

$$R\,2-6: \begin{cases} \bar{i}_g & = \bar{i}_e d_g - \dfrac{v_o d_o d_g}{2f_{sw}L} + \dfrac{v_o \delta_2}{2f_{sw}L} \\ \bar{i}_{out} & = \bar{i}_e d_o - \dfrac{v_g d_o d_g}{2f_{sw}L} + \dfrac{v_g \delta_2}{2f_{sw}L} \end{cases} \tag{11}$$

Thus, the input and the output current can be represented as the sum of the current $\bar{i}_e$, multiplied by d_g and d_o respectively, and an additional current generator labeled $\bar{i}_x$ and $\bar{i}_y$ as follows:

$$\begin{cases} \bar{i}_g & = \bar{i}_e d_g + \bar{i}_x \\ \bar{i}_{out} & = \bar{i}_e d_o + \bar{i}_y. \end{cases} \tag{12}$$

The resulting equivalent non-linear average model of the converter is shown in Fig. 5. From the average model, a simple linearization technique is used to derive the linear small-signal model reported in Fig. 6, in which all coefficients are a function of the considered operating point. In Table I the small-signal coefficients related to Fig. 6 are shown.

IV. SIMULATION RESULTS

In this section, the proposed large-signal model and the related small-signal model are verified with a simulation in Matlab/Simulink using an ideal inductor, capacitor and switching elements. The resistance of the inductor and capacitor and the on-state resistance of the MOSFETs are included in the simulation in the next section. The parameters of the simulation, used for both average and small-signal comparisons, are reported in Table II. State-of-the-art symmetric-on-time single-update digital pulse-width modulators with triangular carriers are used in this paper. With such a modulation method, the input (control) variables are d_g, d_o and β. On the other hand, in the derivations in the previous section, δ_2 is used in place of β, since:

$$\delta_2 = \frac{d_g + d_o + \beta}{2}, \tag{13}$$

which stems from (1).

TABLE II
LIST OF PARAMETERS USED IN THE SIMULATION

Simulation Parameters			
V_g	200 V	C_o	100 µF
f_{sw}	100 kHz	D_g	0.4; 0.5
R_L	20 Ω	D_o	0.6
L	6 µH	β	−0.3; 0.35

A. Average model validation

In order to verify the average model based on (10) we built a circuit simulation using Matlab/Simulink comparing the step response of the proposed large-signal model from Fig. 5 with the switching model. A step excitation of $\Delta d = 5\%$ is applied to the control variable d_o and the response of the output voltage v_o and the $\bar{i}_g$ and $\bar{i}_{out}$ currents are compared. Note that, in order to excite the derived large-signal model, according to (13), it is necessary to simultaneously impose a step change of δ_2 with an amplitude of $\frac{\Delta d}{2}$. The initial circuit parameters are shown in Table II. The chosen steady-state duty-cycles are $D_g = 0.4$ and $D_o = 0.6$ for the region 4-8 and $D_g = 0.5$ and $D_o = 0.6$ for the region 2-6. Fig. 7-8 illustrate the low frequency dynamics of the currents and the output voltage. According to the presented results, the predictions of the proposed model are in agreement with the results from the switching model.

B. Small signal model validation

To verify the proposed small-signal model of the FSBB, this subsection aims to compare the output duty-cycle to output voltage transfer function predicted by the model and the one obtained from the simulated frequency response measurements. This transfer function is obtained from the model in Fig. 6 by substituting $\hat{d}_g = \hat{v}_g = 0$ and $\hat{\delta}_2 = \frac{\hat{d}_o}{2}$, which stems from (13) and $\hat{\beta} = 0$.

From the small-signal model in Fig. 6, the output duty-cycle to output voltage transfer function can be calculated as:

$$G_{dh}(s) = \frac{\hat{v}_o(s)}{\hat{d}_o(s)} = -\frac{V_o}{D_o} \frac{1 - sL\dfrac{a_o + \dfrac{b_o}{2}}{D_o V_o}}{1 + s\dfrac{L}{D_o^2 R_L} + s^2 \dfrac{C_o L}{D_o^2}} \tag{14}$$

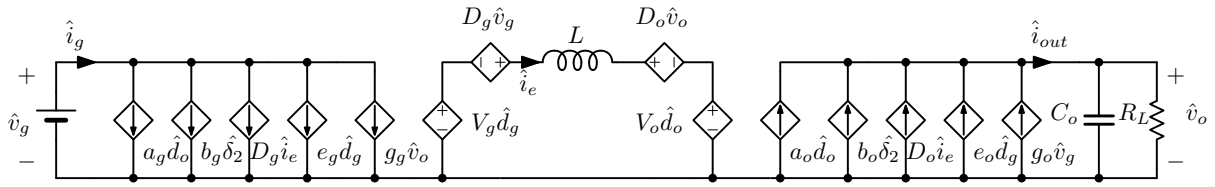

Fig. 6. Linear small-signal model of the FSBB in the Regions 2-6 and 4-8

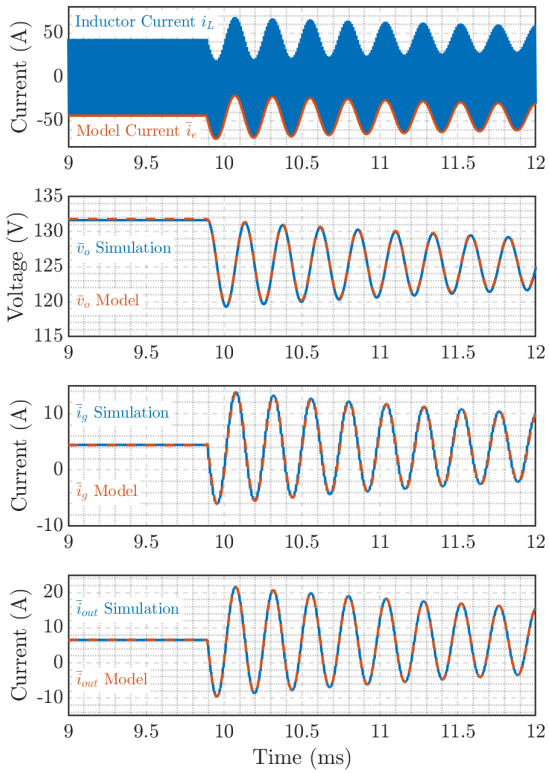

Fig. 7. Response of the switching and the proposed model in the region 8 to a step increment of d_o of 5%. In blue the currents and voltage of the simulation, in dotted orange lines the model quantities

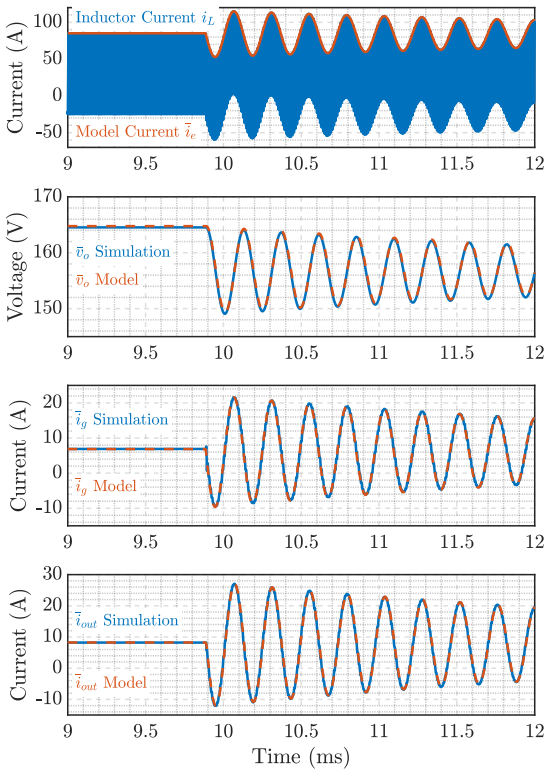

Fig. 8. Response of the switching and the proposed model in the region 6 to a step increment of d_o of 5%. In blue the currents and voltage of the simulation, in dotted orange lines the model quantities

where s is a complex variable of the Laplace transform. Since in this paper, the use of digital pulse-width modulation is considered, when performing frequency response measurements in simulations (and also experiments, addressed in Section V), G_{dh} can not be directly obtained. Rather, the small-signal dynamics of the modulator, G_{mod}, also impacts the measurement. Namely, by measuring the ratio between the output voltage and the perturbed modulation signal, the product of the two transfer functions is obtained (i.e., $G_{dh}(s) \cdot G_{mod}(s)$). The transfer function of the considered DPWM is [9]:

$$G_{mod}(s) = \frac{1}{2}\left(e^{-\frac{s(1-D_o)}{2f_{sw}}} + e^{-\frac{s\,(1+D_o)}{2f_{sw}}}\right) \tag{15}$$

Thus, for the following validations $G_{dh}(s) \cdot G_{mod}(s)$ predicted by (14) and (15) is compared to the simulated frequency response measurements. In simulations, the perturbation of the duty-cycle is created by superimposing a sine wave to the steady-state value of d_o for a frequency sweep between 1 kHz and 50 kHz (Nyquist frequency). Comparison between simulation results and analytical predictions is shown in Fig. 9 for different operating points. The model precisely predicts the response across the whole considered frequency range. The gain at the resonance frequency shows a difference of maximum 0.5dB.

V. Experimental Verification

A laboratory prototype is built using the SiC devices UJ4SC075009K4S for the input leg and UF3SC065007K4S for the output leg. The inductor is based on a PQ32-N97 core with 9 turns, using $800 \times 71\,\mu\text{m}$ litz wire, and an air gap of $1.7\,\text{mm}$. In Table III the circuit parameters are shown. The

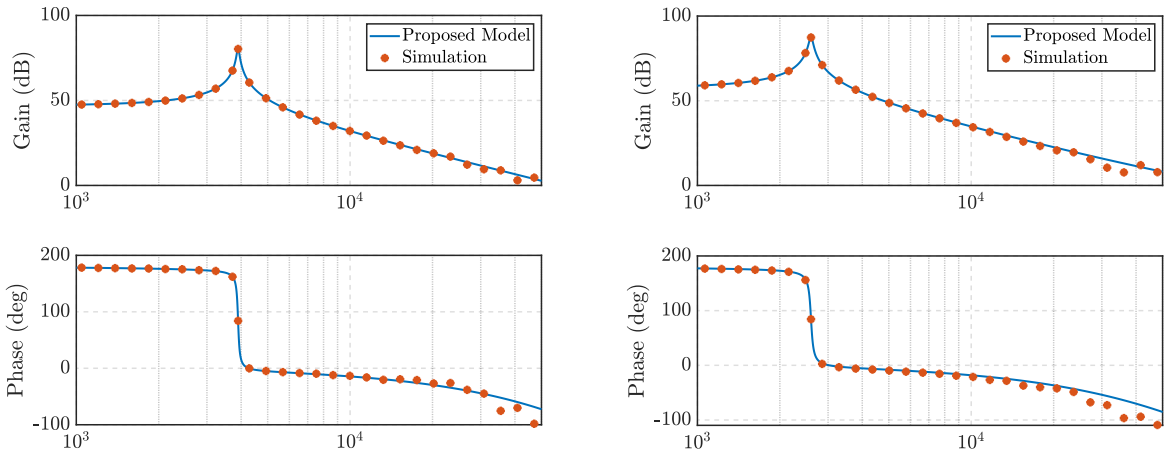

(a) (b)

Fig. 9. Simulation validation of the output duty-cycle to output voltage transfer function. Comparison between frequency response obtained from simulations and the model $G_{dh}(s) \cdot G_{mod}(s)$. The results are given for two operating points: a) Region 4: $D_g = 0.4$, $D_o = 0.6$, $\delta_2 = 0.2$; b) Region 2: $D_g = 0.5$, $D_o = 0.6$, $\delta_2 = 0.2$.

TMS320F28379D is used to implement digital pulse-width modulation.

Firstly, the experimentally obtained time domain waveforms of the input and output switching node voltage v_1 and v_2, and inductor current i_L of the tested FSBB are shown in Fig. 10, for two different operating points. Fig. 10 a) corresponds to operating region 2 (step-up case), whereas Fig. 10 b) corresponds to operating region 8 (step-down case).

For these two operating points, frequency response measurements are performed in order to experimentally validate the output duty-cycle to output voltage transfer function. The procedure used is explained in the following. The Bode functionality of the Rohde&Schwartz RTA4004 oscilloscope was used with which it is possible to calculate the Bode plot of the transfer function of two probe signals. The waveform generator signal of the RTA4004, taken as input of the Bode plot, after first filtering and scaling, is acquired by the analog to digital converter of the microcontroller TMS320F28379D and is properly scaled and processed to inject a sinusoidal perturbation on the duty-cycle of the output leg. The output voltage v_o of the FSBB is chosen as the second signal. Perturbing the circuit, the oscilloscope automatically measures the Bode plot. The proceeding is described in the following steps:

- **Calibrations step**: by connecting the two probes together, the measurement offset, which will later be subtracted from the main results, is measured;
- **Measurement step**: using the Bode application, the frequency response of the target transfer function is measured;
- **Post processing step**: the results from the previous step are post-processed, taking into consideration the microcontroller operation and subtracting the offset calculated from the calibration step.

In this way, experimentally measured perturbed modulation signal to output voltage transfer function is obtained.

TABLE III
PARAMETER VALUES OF THE CIRCUIT

V_g	50 V	C_o	25 µF
f_{sw}	100 kHz	R_{ind}	16 mΩ
R_L	45.6 Ω	R_C	20 mΩ
L	6.4 µH	t_d	120 ns

For the purposes of benchmarking, it is of interest to compare experimental with simulated frequency response measurements. Differently from the simulation model used in the previous section, now the inductor resistance, R_{ind}, MOSFETs on-resistance, R_{dson}, capacitor ESR, R_C, and dead-time, t_d, are included in the simulation, in order to account for some of the converter non-idealities present in the experimental setup. In the simulation, the resistances are simply added to the corresponding blocks and the dead-time effect is realized by delaying the rising edges of all of the MOSFET gate signals.

The proposed small-signal model is also enhanced to take the aforementioned non-idealities into account, as explained below. To account for the parasitic resistances, the circuit from Fig. 5 is modified such that the resistances of inductor and MOSFETs are considered in series with the inductor and the resistance of the capacitor in series with the latter. Therefore, the impedances of inductance and capacitance become $Z_L = sL + R_{ind} + R_{dson1} + R_{dson2}$ and $Z_{out} = 1/sC_o + R_C$, respectively, where R_{dson1} and R_{dson2} are the on-resistances of the first and second leg. This yields the following output

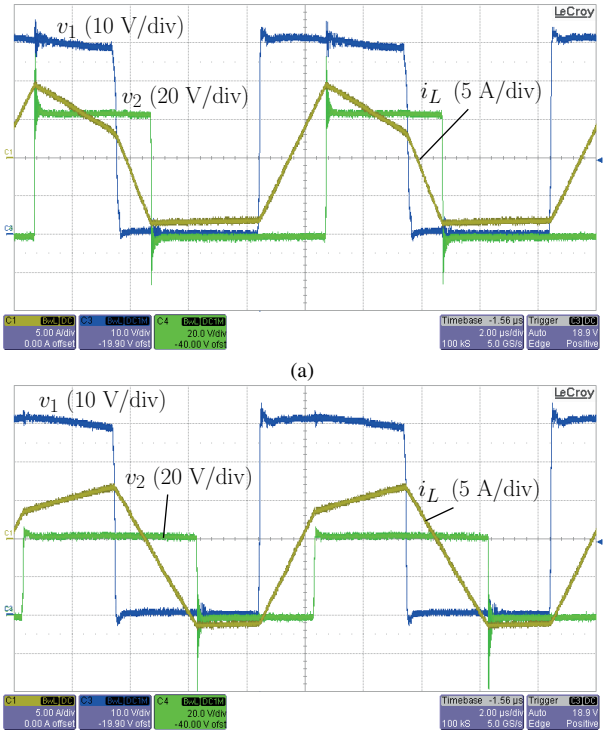

Fig. 10. Input and output switching node voltage v_1 and v_2, and inductor current i_L of two operating points: (a) $D_g = 0.5$, $D_o = 0.4$, $\delta_2 = 0.23$ and (b) $D_g = 0.5$ $D_o = 0.6$, $\delta_2 = 0.3$.

duty-cycle to output voltage transfer function:

$$G_{dh}^{par}(s) = \frac{\hat{v}_o(s)}{\hat{d}_o(s)} = Z_{out} \frac{a_o + \frac{b_o}{2} - \frac{c_o V_o}{Z_L}}{1 + \frac{c_o D_o Z_{out}}{Z_L}} \qquad (16)$$

The dead time is taken into account as a reduction of the effective duty-cycles D_g and D_o.

Comparison between the proposed small-signal model which takes into account converter non-idealities and the previously explained experimental and simulated frequency response measurements is provided in Fig. 11, for the step-up and step-down case. Simulation results match the analytical predictions in the whole considered frequency range. Around resonant frequency, a slightly higher damping is observed in the experimental results. This is assumed to be related to the non-linear damping effect of the dead-time as reported in [10] and to the core and switching losses, none of which are taken into account neither in the model nor the simulation. A more detailed analysis of these effects will be addressed in future work.

VI. Conclusions

This paper has presented a non-linear average model and the corresponding small-signal model of the four-switch buck-boost converter under both duty-cycle and phase-shift modulation. This paper focused on two specific regions of operation that allow zero voltage switching of all four switches. In the presented modelling approach, the average inductor current is

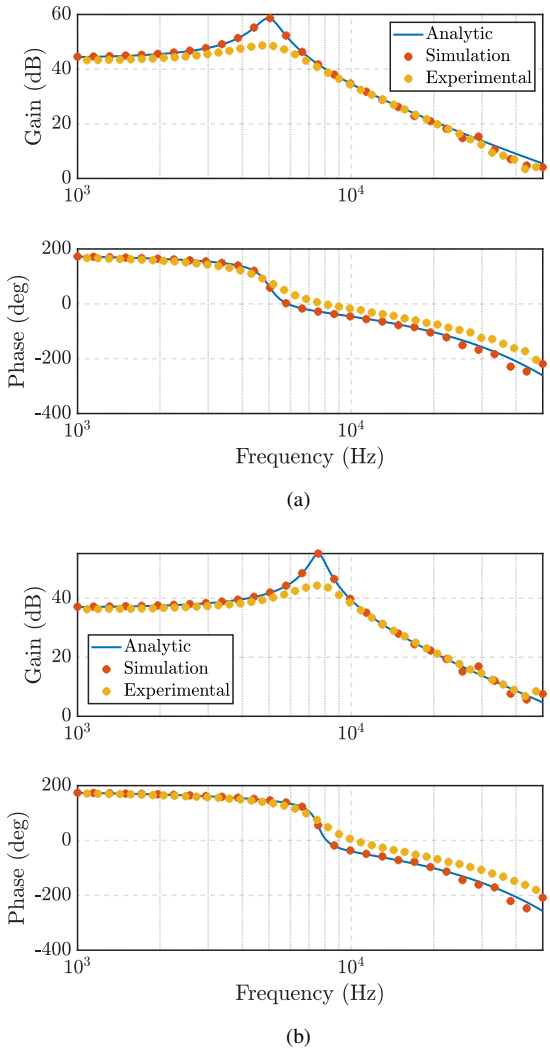

Fig. 11. Verification of the output duty-cycle to output voltage transfer function. Comparison between frequency response obtained from simulations, preliminary experimental results and model $G_{dh}^{par}(s) \cdot G_{mod}(s)$. The results are given for two operating points: (a) $D_g = 0.5$, $D_o = 0.4$, $\delta_2 = 0.23$ and (b) $D_g = 0.5$ $D_o = 0.6$, $\delta_2 = 0.3$.

not one of the state variables, and instead, a new state variable is introduced. The simulation and experimental results have verified the non-linear large-signal and linearized small-signal models of the four-switch buck-boost converter. Compared to the analytical predictions and simulation results, experimental frequency response measurements exhibit a slightly higher damping around the resonant frequency. This is assumed to be due to the effects of the losses in core of the inductor and the non-linear damping of dead-time, which will be analyzed in future work.

References

[1] X. Sun, J. Qiu, X. Li, B. Wang, L. Wang, and X. Li, "An improved wide input voltage buck-boost + LLC cascaded converter," in *2015 IEEE Energy Conversion Congress and Exposition (ECCE)*, 2015, pp. 1473–1478.

[2] Q. Qian, Q. Liu, H. Li, S. Xu, and W. Sun, "Optimal Phase Shift Control Strategy of Buck-Boost Integrated LLC Converter Achieving Wide Input Voltage Range, MHz-frequency and High Efficiency," in *2020 IEEE*

Applied Power Electronics Conference and Exposition (APEC), 2020, pp. 922–926.

[3] Q. Liu, Q. Qian, B. Ren, S. Xu, W. Sun, and L. Yang, "A Two-Stage Buck-Boost Integrated LLC Converter With Extended ZVS Range and Reduced Conduction Loss for High-Frequency and High-Efficiency Applications," *IEEE Journal of Emerging and Selected Topics in Power Electronics*, vol. 9, no. 1, pp. 727–743, 2021.

[4] N. Zanatta, T. Caldognetto, G. Spiazzi, and P. Mattavelli, "Analysis and performance evaluation of a two-stage resonant converter for wide voltage range operation," in *2022 IEEE Applied Power Electronics Conference and Exposition (APEC)*, 2022, pp. 1141–1147.

[5] X. Ren, X. Ruan, H. Qian, M. Li, and Q. Chen, "Three-mode dual-frequency two-edge modulation scheme for four-switch buck–boost converter," *IEEE Transactions on Power Electronics*, vol. 24, no. 2, pp. 499–509, 2009.

[6] H. Xu, F. Wang, and H. Guo, "Short-time scale mode transition control of the four-switch buck-boost converter," in *2021 11th International Conference on Power and Energy Systems (ICPES)*, 2021, pp. 62–67.

[7] Y.-J. Lee, A. Khaligh, and A. Emadi, "A compensation technique for smooth transitions in non-inverting buck-boost converter," in *2009 Twenty-Fourth Annual IEEE Applied Power Electronics Conference and Exposition*, 2009, pp. 608–614.

[8] C.-W. Chen, K.-H. Chen, and Y.-M. Chen, "Modeling and controller design of an autonomous pv module for dmppt pv systems," *IEEE Transactions on Power Electronics*, vol. 29, no. 9, pp. 4723–4732, 2014.

[9] D. Van de Sype, K. De Gusseme, A. Van den Bossche, and J. Melkebeek, "Small-signal laplace-domain analysis of uniformly-sampled pulse-width modulators," in *2004 IEEE 35th Annual Power Electronics Specialists Conference (IEEE Cat. No.04CH37551)*, vol. 6, 2004, pp. 4292–4298 Vol.6.

[10] M. Berg, T. Messo, T. Roinila, and P. Mattavelli, "Deadtime impact on the small-signal output impedance of single-phase power electronic converters," in *2019 20th Workshop on Control and Modeling for Power Electronics (COMPEL)*, 2019, pp. 1–8.